

Characterization of a Hadamard transform time-of-flight mass spectrometer

Ansgar Brock, Nestor Rodriguez, and Richard N. Zare^{a)}

Department of Chemistry, Stanford University, Stanford, California 94305

(Received 17 March 1999; accepted for publication 29 November 1999)

A pseudorandom time-of-flight method (also called the cross-correlation method) has been used to perform time-of-flight mass spectrometry with a duty cycle of 50%. Modulation of an ion beam is accomplished by deflecting the ion beam with an interleaved comb of oppositely charged elements. Maximum-length pseudorandom sequences based on Hadamard-type difference sets are produced by feedback shift register circuitry and used for ion beam modulation. The inverse transformation of the recorded signal is carried out speedily with the help of the fast Hadamard transform, which allows real-time monitoring of the mass spectrum. The components of the instrument are described, and its performance is characterized. Trajectory simulations are found to be in good agreement with experimental findings, which aids in understanding the modulation dynamics. It is found that the wire comb modulator can be modeled as a set of ideal deflection plates of length $0.875 l$, where l is the spacing between oppositely charged wires. © 2000 American Institute of Physics.

[S0034-6748(00)00403-2]

I. INTRODUCTION

Time-of-flight (TOF) analysis has found widespread application because particle velocity, energy or momentum, and mass can be determined from such an experiment by constraining the appropriate parameters for the experiment. Examples of the application of the technique are found in neutron and molecular beam scattering of neutral particles,¹⁻³ where it is the method of choice for extracting the desired velocity information. This method has also been applied to charged particles, and examples are photoelectron spectroscopy⁴ and time-of-flight mass spectrometry (TOFMS).⁵⁻¹⁰ Time-of-flight mass spectrometers have the very desirable characteristic of high ion transmission, high repetition rate, good resolution, and modest cost,⁵ which makes them very attractive as a mass-sensitive detector in analytical instrumentation. Application to analytical instrumentation was, until recently, somewhat hampered by the fact that most analytical ion sources produce continuous ion beams. The pulsed operation of a conventional time-of-flight mass spectrometer caused the duty cycle to be rather low and TOFMS could not live up to its promises.⁸

The interface design between a continuous ion source and a time-of-flight mass spectrometer must overcome two problems. One is bringing the ions with as little spatial and kinetic energy spread as possible into the spectrometer for the purpose of achieving high resolution of the masses. The other is using as much of the ions supplied by the continuous source as possible without compromising on the first requirement so that a high duty cycle can be achieved. Today, the preferred and highly refined solution to these problems is orthogonal acceleration (OA).¹¹ By OA it is meant that the ion beam emanating from the ion source enters the time-of-flight instrument at a right angle with respect to the flight axis of the ions in the spectrometer. This geometry allows a

low spatial and kinetic energy spread to be achieved. The duty-cycle objective is met by extending the width of the extraction region so that a larger fraction of the ion beam coming from the source can be sampled. Active ion storage can be achieved by accumulation of ions in an ion guide connecting the ion source and the extraction region during the time an extracted ion packet disperses in the instrument. Orthogonal acceleration was perfected in recent years, and typical duty cycles are 20%–30% with a resolution of 10 000.¹² Most recent results indicate that much higher resolving powers might be achievable.¹³

Bakker^{14,15} and later Yefchak *et al.*¹⁶ suggested for interfacing a continuous ion source with TOFMS the production of ion packets by modulation of the continuous beam. This interface elegantly circumvents many of the problems associated with the initial spatial distribution of the ions in the extraction region. The major disadvantage of this solution is the low ion extraction duty cycle. The duty cycle is given by the pulse width generated by the method divided by the record length of one time-of-flight distribution. It is typically on the order of 10^{-4} .¹⁶

Interestingly, this low duty-cycle problem was solved long ago in neutron scattering TOF experiments. There the solution is known under the name of pseudorandom or cross-correlation time-of-flight analysis and allows for duty cycles of 50%.¹⁻³ In the following we describe the implementation of this method in TOFMS. The name Hadamard transform time-of-flight mass spectrometry (HT-TOFMS) was chosen for this implementation for several reasons. The mathematics involved in the analysis of this type of experiment is based on difference sets.¹⁷ Difference sets can be grouped into different classes. To our knowledge all the difference sets used to date for implementing TOF experiments of the multiplexing employ Hadamard-type difference sets. Consequently, the analysis of this type of experiment is based on Hadamard matrices and the computations are carried out expediently with the help of the fast Hadamard transform (FHT).¹⁸ Fur-

^{a)}Electronic mail: zare@stanford.edu

ther, the same multiplexing scheme based on Hadamard difference sets is known in optical spectroscopy under the name Hadamard spectroscopy^{18,19} and contrasted there with the much more common methods of Fourier multiplexing.^{20–22}

A rather limited number of attempts have been made to implement multiplexing in TOFMS. For a short historical survey, the reader should consult a recent publication where this subject was reviewed.⁷

II. DISCUSSION OF THE METHOD

A. Theoretical background

In the following the principle of operation of the Hadamard transform time-of-flight method is illustrated to give the reader unfamiliar with this type of experiment some background. For a more detailed description of the underlying mathematical treatment reference is made to a number of excellent publications on pseudorandom time-of-flight analyses, as practiced in neutron and reactive scattering.^{3,17,23–26} It should be noted that these treatments consider the case of a particle counting experiment and assume therefore shot noise to dominate. The same is true for HT-TOFMS and the derived results are therefore also valid for this application. The mathematical procedures for actually carrying out the inverse transform of a signal waveform by FHT might be most easily understood by referring to the book of Harwitt and Sloane,¹⁸ which discusses the optical techniques.

Modulation of an ion beam on a time scale that is short compared to the drift time of the ions through the analyzer produces a rather complex signal at the detector. This signal is the convolution of the modulation waveform with the time-of-flight distribution. Mathematically an on/off modulation is described by a sequence of elements a_i that are either 0 or 1. The sequence of 0's and 1's used for modulation is logically chosen in such a way as to minimize the error in the TOF distribution to be determined.¹⁷ A single 1 in the sequence corresponds to turning the beam on for 1 time unit, which is the time resolution of the instrument. And this time unit is also the bin width in which the signal is usually sampled. The individual ion packets produced by beam modulation are independent of each other and disperse according to their mass-to-charge ratios as ions drift through the instrument. This behavior produces a detector output that can be pictured as the overlap of many identical TOF spectra that are shifted in time with respect to each other. The time or phase shift of the individual TOF distributions is contained in the modulation sequence employed. The observed signal \mathbf{Z} is the product of a matrix \mathbf{S} describing the modulation and the time-of-flight distribution \mathbf{F} , which is the function to be determined as follows:

$$\mathbf{Z} = \mathbf{S} \times \mathbf{F} + \mathbf{U}. \quad (1)$$

In addition, the signal \mathbf{Z} also contains a time-independent background \mathbf{U} arising from dark counts and so on. The time-independent background \mathbf{U} is usually not measured and therefore not subtracted from \mathbf{Z} before multiplying it by \mathbf{S}^{-1} , the inverse of \mathbf{S} , to recover the TOF distribution \mathbf{F} as shown in:

$$\mathbf{F} = \mathbf{S}^{-1} \times \mathbf{Z}. \quad (2)$$

The matrix \mathbf{S} is a circulant and so is \mathbf{S}^{-1} . The columns of \mathbf{S} are the modulation sequence shifted by the column index with respect to the first column. A solution to the minimum problem of the error in \mathbf{F} is easily constructed when a difference set is given.¹⁷ The difference set allows the construction of the modulation sequence, which will always be a pseudostatistical binary sequence. Having the modulation sequence at hand, the matrices \mathbf{S} and \mathbf{S}^{-1} can be readily computed.

It is important to note that a very large number of difference sets of the Hadamard type exist.¹⁷ Sequences constructed from these difference sets have the properties of being of length $N = 2^m - 1$, where m is an integer. From these N elements 2^{m-1} are 1, and $2^{m-1} - 1$ elements are 0. It follows immediately that the duty cycle will be $\sim 50\%$ for large N . Construction of the inverse of \mathbf{S} is accomplished by replacing all 0's in \mathbf{S} by $-1/k$ and all 1's by $1/k$, where k is the number of 1's in the pseudorandom sequence. Error analysis shows that when these sequences are used the error in a spectral element of the recovered TOF distribution is independent of the intensity of the elements. To state this result differently, the error is uniformly distributed over the spectrum. Furthermore, it was shown that a 50% duty-cycle sequence is superior to sequence of smaller duty cycle for cases in which the time-independent background is larger than one-half the signal \mathbf{F} .¹⁷ But, the variance in the worst case will only be a factor of 2 higher than for a pseudorandom sequence having the optimum duty cycle.^{2,17} The small gain that can be achieved by using the optimum duty cycle sequence does not usually warrant the effort of finding and implementing it. Additionally, the straightforward generation of pseudorandom sequences based on Hadamard difference sets results in their exclusive use. In practice, it is not even necessary to construct the desired pseudorandom sequences from difference sets. Maximum length pseudorandom sequences (MLPRS) are readily generated by feedback shift register circuitry,^{18,22,27–29} which is the approach chosen in this implementation of HT-TOFMS.

B. Operational modes

Figure 1 illustrates two operational modes of the HT-TOFMS instrument. In "the gate mode" the beam is turned on and off for the whole duration of a 1 in the sequence as described in the theoretical background and as shown in Fig. 1(a). The time resolution in this mode is given as 1 time unit, and sampling of the signal must be done in integer fractions of a time unit to be able to recover the spectrum. The largest allowed sampling bin width is therefore 1 time unit. Sampling of the signal waveform into bins of integer fractions of the unit time requires a corresponding increase in the total number of sampling bins to cover the whole waveform. The recovery of \mathbf{F} from the recorded signal \mathbf{Z} after sampling in bins smaller than the maximum size requires that the inverse transform of the signal be carried out in sets of every second, third, or whatever multiple that was used in increasing the sampling density. After transformation the individual sets must be again interspersed to form the TOF distribution \mathbf{F} . This procedure will increase the definition of individual

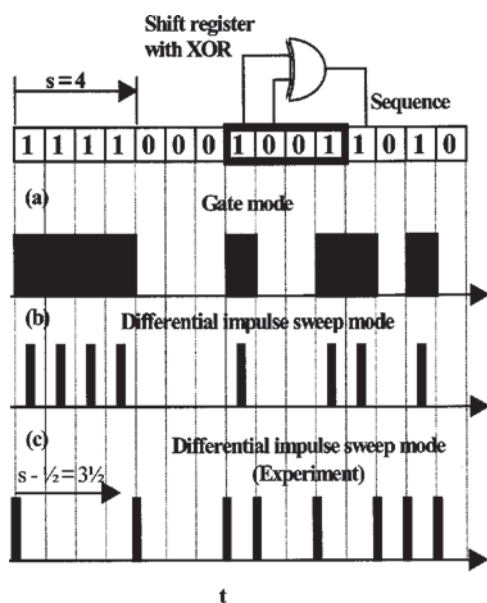


FIG. 1. Operational modes of the Hadamard transform time-of-flight mass spectrometer. The sequence generated by a four-bit shift register with XOR feedback of bits three and two is shown at the top. (a) Gate mode and unit time resolution, (b) differential impulse sweep mode, and (c) modulation function used in the experiment. The introduced phase shift $s - \frac{1}{2} = 3\frac{1}{2}$ sequence elements between gate and differential impulse sweep mode is indicated (s is the distance between the largest blocks of consecutive 1's and 0's in the sequence).

peaks, but it is not able to increase the time or mass resolution of the experiment. To increase the time resolution, a shortening of the unit time interval is necessary in the gate mode. The duty cycle will be unaffected by shortening the unit time interval and will still be 50%, but the cycle time, and therefore the mass range covered for a given sequence, will be compressed accordingly.

In practice, short ion packets are readily produced by use of transient effects, namely the sweeping of the beam over a slit as done in a beam-modulated time-of-flight mass spectrometer.¹⁴⁻¹⁶ The resulting transient or pulse is usually much shorter than the time necessary to repeat it so that the duty cycle is less than the 50% value achieved in the gate mode. Nevertheless, the duty cycle can still be comparatively high, and the analysis of the experiment is essentially unchanged, as will be shown. In Fig. 1(b) short pulses have replaced the unit time pulses [Fig. 1(a)] produced by running the instrument in the gate mode. It is immediately clear that the higher time resolution from the shortened pulses can only be fully seen in the final spectrum if the sampling bin width is reduced to at least the transient pulse width, which is smaller than a unit time element of the sequence. The signal waveform needs to be sampled therefore as described above for increasing the peak definition in the gate mode. Thus, sampling needs to take place into bins of integer fractions of the unit time element of the logic sequence and the total number of sampling bins to cover a full cycle of the waveform must be increased proportionally. Recovery of \mathbf{F} from the recorded signal \mathbf{Z} is achieved by carrying out the inverse transform of the proper subsets of bins and interspersing after transformation.

Figure 1(c) illustrated what this beam modulation actu-

ally looks like in the experiment. Because beam sweeping is achieved by inversion of the potentials applied to the modulation wire sets, a short pulse is produced at any 0 to 1 or 1 to 0 transition in the logic sequence. It is then obvious that the modulation sequence appears as shown in Fig. 1(c), which is different from those in Figs. 1(a) and 1(b). The question arises of how to recover the TOF distribution from this type of modulation. Fortunately, the mathematical properties of MLPRS's produced through shift register generation dictate that the modulation sequences of Figs. 1(a) or 1(b) and that of Fig. 1(c) are identical. They only look different because a phase shift has been introduced. This result might seem surprising, but it is well documented in the literature.^{24,26} The value of this phase shift is $s - 1/2$ sequence elements, where s is the number of sequence elements between the largest group of consecutive 1's and the largest group of consecutive 0's. For the shift register sequence shown in Fig. 1(a) the largest block of consecutive 0's follows immediately after the largest block of consecutive 1's. The number of s is therefore just the size of the largest block of consecutive 1's, which is 4 and the phase shift $s - 1/2$ is computed to $3\frac{1}{2}$ elements. Shifting of the sequence shown in Fig. 1(c) by $3\frac{1}{2}$ elements to the right as indicated by the arrow and keeping in mind that the sequence is cyclic, meaning it flips around at the end, produces the sequence in Fig. 1(b), *vide infra*. Therefore, the TOF distribution can be recovered with the same FHT that is used to recover the spectra modulated in a fashion like that shown in Figs. 1(a) and 1(b) except that a correction for the phase shift needs to be made either before or after back transformation. This property of maximum length pseudorandom sequences produced by shift register circuits is of great importance because it can also explain the appearance of negative image peaks for cases in which the bin width for modulation according to Fig. 1(a) is systematically too large or too small.^{24,26} This type of artifact is typically observed in our experiment when the signal is averaged for long times to increase the signal-to-noise ratio (SNR). Whereas the statistical noise reduces with averaging, the nonstatistical noise originating from this artifact does not, and it will ultimately dominate.

III. INSTRUMENTATION

Figure 2 shows a schematic diagram of the Hadamard transform time-of-flight mass spectrometer equipped with an electrospray ionization (ESI) source. In operation the ion beam generated by the electrospray source is extracted and accelerated from the octopole ion guide by a three-element lens. The potentials of the lens elements are adjusted to values that produce a parallel beam at the modulator, which floats together with the third lens element at the flight tube potential. The parallel beam is steered, with the help of two sets of deflection plates, through the ion mirror and onto the detector.

Application of equal magnitude but oppositely signed potentials to the grid of wires forming an interleaved comb causes the ion beam to be split into two slightly deflected beams. This slight deflection is sufficient to cause the de-

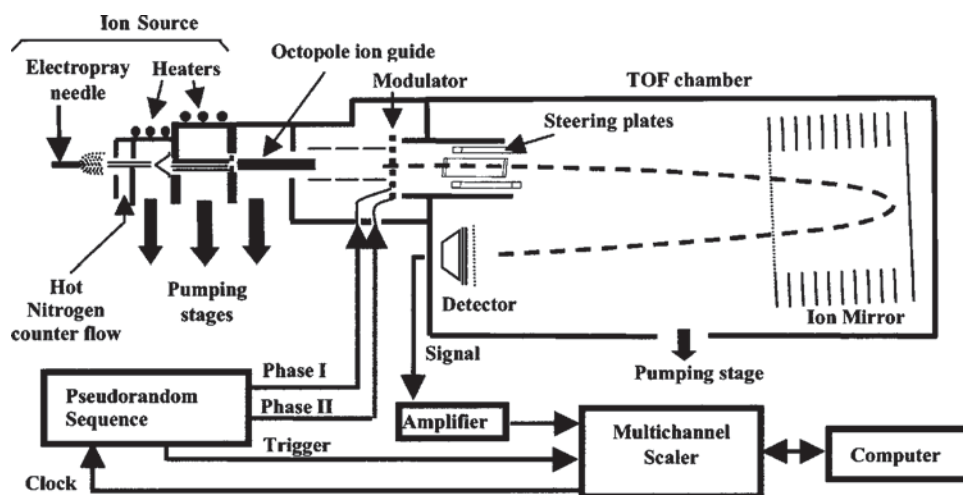


FIG. 2. Experimental setup of the Hadamard transform time-of-flight mass spectrometer.

flected beams to strike the sides of a slit placed in front of the detector, which corresponds to the beam off state or a 0 in the modulation sequence. The undeflected beam passing through the detector slit onto the detector represents the beam on state or a 1 in the modulation sequence. Bringing both alternating sets of wires to the same potential produces it. The instrument is composed of four main functional blocks, the ion source and imaging optics, the modulator, the vacuum system and detector, and the modulation and data acquisition electronics. These functional blocks are discussed in more detail in the following.

A. Electrospray ionization source and ion optics

The layout of the ion source is similar to a collisional damping interface that was described by Krutchinsky *et al.*³⁰ in great detail. A syringe pump (Harvard Apparatus, Mo. 11) supplies analyte solutions with flow rates of 0.5–5 $\mu\text{l}/\text{min}$ to the electrospray tip, which is typically held at a potential of 1.5–3 kV to achieve a stable electrospray. A heated stainless steel capillary [length 9 cm, inner diameter (i.d.) 0.5 mm] provides for desolvation and transport of the spray into the first differentially pumped region. It also serves as the counter electrode of the spray. The capillary is maintained typically at temperatures between 120 and 220 $^{\circ}\text{C}$ to allow for efficient desolvation while the ion source body is heated to 120 $^{\circ}\text{C}$ by an adapted 400 W diffusion pump heater and heating tapes. All the elements of the ion source are electrically isolated from each other and ground, which allows easy adjustment of the potentials between the individual elements by floating them to the appropriate potentials. Typical potentials with respect to ground are given in Table I for normal and ion source collisional induced dissociation (CID) operation. The pressure in the first differential pump region is adjustable by throttling a 13 s^{-1} mechanical pump that evacuates the region. The distance between the heated capillary and the skimmer plate is adjustable, but it is usually fixed to be around 10 mm. The opening in the skimmer plate is 1.6 mm in diameter. The second differentially pumped region is 90 mm from the skimmer plate to the lens plate. A quadrupole made from 7.95 mm diameter stainless steel rods with a length of 86.5 mm allows efficient trapping and transport of ions through this region. The quadrupole is mounted onto the

lens plate and has an inner diameter of 6.43 mm. A pressure between 1.3×10^{-1} and 1.3×10^{-3} mbar is maintained in the quadrupole region by a 150 s^{-1} turbomolecular pump. The third differential pump region is exhausted by a pump stack consisting of gate valve, water-cooled baffle, and diffusion pump with an effective pump speed of 1500 s^{-1} . The pressure in this region is typically 2.5×10^{-5} mbar. Ions are transported through this region by an octopole ion guide (182 mm in length) that extends into the time-of-flight chamber, where the acceleration and imaging optics are located. The guide is made from 3.175 mm diam stainless steel rods having an inner diameter of 6.7 mm. The two ion guides are driven by power supplies (Extranuclear Laboratories, Mo. 011; Q -head, Mo. 13+Mo. 15) with frequencies of ~ 1.2 MHz for the quadrupole and ~ 700 kHz for the octopole, respectively. Both ion guides operate in the radio frequency (rf)-only mode. The radio frequency amplitude is adjusted for optimum ion signal and is typically ~ 400 V for the quadrupole and ~ 750 V for the octopole. Under these conditions suppression of ion signals below 200 amu is observed. Acquisition of mass spectral data in the low-mass region requires the rf amplitude to be lowered.

B. Time-of-flight mass spectrometer

The ions are accelerated to final energies of up to 1.5 kV. Ions are extracted from the octopole ion guide by a high negative potential of typically -2 kV on the first accelerat-

TABLE I. Potential settings for normal and CID operation of the Hadamard time-of-flight mass spectrometer.

Element	Typical float potentials in V	
	Normal operation	Ion source (CID)
Spray needle	1500–3500	1500–3500
Capillary	0	500
Skimmer plate	0	15
Quadrupole	0	0
Float plate	0	0
Octopole	-2	-2
1st lens (E_{beam} 1250 eV)	-2000	-2000
2nd lens (E_{beam} 1250 eV)	290	290
3rd lens (E_{beam} 1250 eV)	1250	1250

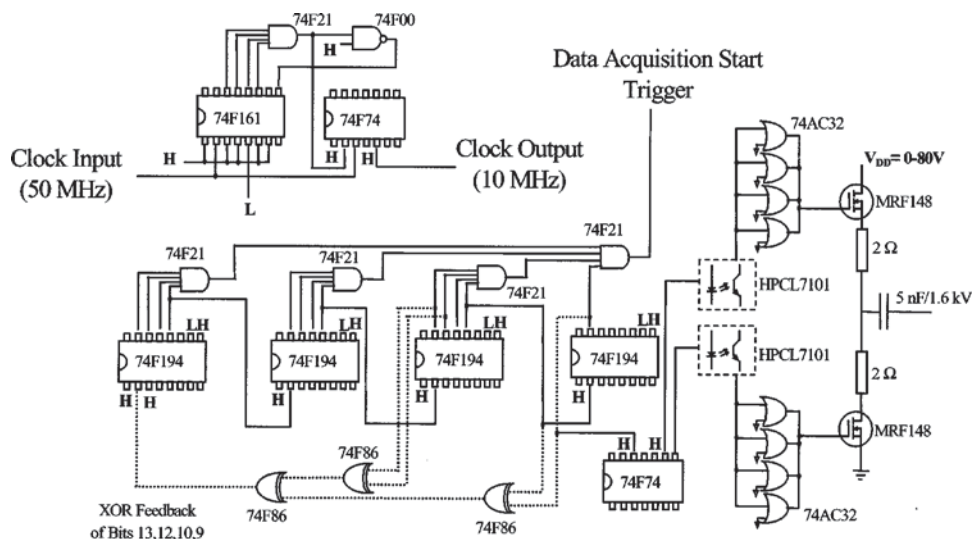


FIG. 3. Circuit diagram of the pseudorandom sequence generator. Signal lines are for the case of a 13-bit generator, clocked at 10 MHz. Only one power amplifier stage is drawn.

ing lens element. The spacing between the three lens elements is 2 mm. The lens elements are identical cylinders with an i.d. of 25 mm, an outer diameter (o.d.) of 49 mm, and a length of 41 mm. SIMION 6.0³¹ simulations show that the high potential on the extractions lens element produces a focal point inside the octopole. The potential on the second lens element is adjusted to a value that produces a parallel beam at the modulator, which floats together with the third lens element at the flight tube potential. Simulations show that the ion beam passes through the focusing optics as a rather tight beam, which is less than 6 mm in diameter at any position inside the optics. Two sets of deflection plates are positioned after the grid modulator. The plates are 63.5 mm wide and 93.1 mm long. Deflection potentials are applied symmetrically with respect to the ion beam potential to keep the centerline at beam potential.

The single-stage ion mirror is constructed from 39 gold-plated titanium frames. The frames are square with an outer frame dimension of 149 mm and square centered cutout of dimension 117 mm. Frames are spaced 10 mm apart by four slotted synthetic glass–mica composite rods. Field sagging at the entrance of the reflector is suppressed by 20 μm gold-plated tungsten wires soldered at a distance of 0.8 mm to the first frame. The end plate is massive. For ion detection a standard dual microchannel plate detector is employed with 1 kV applied across each channel plate.

The time-of-flight chamber is a rectangular box manufactured from 304 stainless steel plates of 6.35 mm thickness, which are reinforced by welding steel angle to the outside surface. The removable top lid is sealed to the rest of the chamber by a Viton o-ring made from 5 mm diameter cord. The inside dimensions of the box are 1003 \times 305 \times 305 mm. The chamber is evacuated by a 1500 $\ell\text{ s}^{-1}$ turbomolecular pump to a base pressure of $\sim 4 \times 10^{-7}$ mbar with no gas load coming from the electrospray ion source and $\sim 9 \times 10^{-7}$ mbar under ESI operation.

The ion mirror and deflection plates are mounted on a perforated stainless steel plate that is electrically isolated from the chamber by ceramic posts. A box also made from perforated stainless steel covers all of the ion optics inside

the chamber and forms, together with the base plate, a cage that is floated to the ion beam potential.

C. Modulator

Interleaved combs were used initially for electron deflection.^{32,33} Weinkauff *et al.*³⁴ were the first to apply them in mass spectrometry and others have used them in modified forms^{35,36} for mass gating experiments. In the application described here, the device is employed as a replacement for the deflection plates used in beam modulation TOFMS for switching or pulsing of the ion beam. This application is rather different from the gating applications of spatially mass separated ion packets reported so far.

The frame of the modulator is made from a piece of double-sided circuit board. The outer dimensions are 65 \times 60 mm² with a centered square cutout of 44 \times 44 mm². The wires (20.3 μm in diameter) consist of gold-plated tungsten, and they are stretched along the larger dimension of the frame. Alternating wires are spaced at a distance of 158.7 μm . The device has quite a large active area of about 25 \times 25 mm². Each of the two interspersed wire sets is soldered to electrode pads on the frame, where contact with the driver is made. The wires are held in position by polymethylacrylamide spacers glued to the wires.

D. Pseudorandom sequence generator and power amplifier

Figure 3 presents a circuit diagram of the pseudorandom sequence generator and power amplifier. Only the signal lines essential for the understanding of the operation of the circuit are indicated. The circuit is constructed from *F* logic elements, which allow an upper clock speed of around 100 MHz. For proper operation of the experiment synchronization of modulation and data acquisition is necessary. This synchronization is achieved by running the sequence generator from the internal clock of a multichannel scaler (EG&G Ortec, Mo. T914), which was customized by the manufacturer to provide a 50 MHz clock output. The clock output of the multichannel scaler is divided down with the help of

a four-bit synchronous presentable binary counter (MC74F161). Frequency division by a factor of 5 is achieved by programming the counter to start counting at 11 by setting the internal shift register of the counter over its inputs. Each clock pulse increments the counter by 1 until it reaches 15, after which it would overflow and continue to count from 0. Overflow is prevented by decoding the shift register outputs with a four-input AND gate (74F21). The output of the AND goes to a logic high level when the register reaches the binary state corresponding to 15. The decoding AND output is inverted by a NAND gate (74F00), which pulls the parallel load input (\overline{PE}) of the counter to logic low. As a result of the logic low on the \overline{PE} input the next clock pulse causes loading of the register with the value preset at the inputs, instead of overflowing to state 0. In this way the register cycles through states 11–15 and a parallel load state, which results in a division by five. Other settings of the inputs on the presentable counter allow division of the input clock by other integer values, so that the clock period is adjustable starting from 20 ns in increments of 20 ns up to 320 ns. The divided clock output could be taken directly from the decoding AND output, but this choice could lead to erroneous clock pulses when the binary counter changes states. To prevent this condition the output is run through a D flip-flop (74F74). The divided clock output is then fed to the clock inputs of the universal shift registers (74F194) and another D flip-flop (74F74) used as phase splitter at the output of the sequence generator. The clock lines are not shown for clarity.

A 13-bit shift register is constructed by chaining together four universal four-bit bidirectional shift registers (74F194), as shown in Fig. 3. The output for the last bit of register one is chained to the data shift right (D_{SR}) input of register two and so on. The feedback circuit is closed by generating the input for register one by modulo-2 addition of bits 13, 12, 10, and 9. Modulo-2 addition is implemented with three exclusive-OR (XOR, 74F86) gates, which first add bit 13 to 12 and 10 to 9 and then the result. The outcome of this modulo-2 addition is fed back into the D_{SR} input of register one, which closes the feedback loop. The last three bits of the fourth register is not used in the circuit shown, but they allow for expansion to sequences of a maximum length of 65 535. The 13-bit register produces a MLPRS of 8191 elements. The setting of the master reset input (\overline{MR}) to high and the select inputs (S_0, S_1) to high and low respectively causes the registers to shift right at the rising edge of each clock pulse. The sequence is taken from the output of bit 13, which is the first bit of shift register four. It would be equally possible to take the sequence from any other bit of the 13-bit register. During operation the 13-bit register cycles through any possible state exactly one time with the exception of all zero bits. This cycling produces a maximum length sequence of $2^{\text{number of bits}} - 1$ or 8191 for n equal to 13 bits. The state with all zero bits is not allowed because then XOR feedback would produce only more 0's and no longer any 1's. After turning the power on, the circuit does not usually produce the desired sequence, because the registers seem to be biased to initialize themselves to this all-zero state. This cycle of producing only zeros is broken, causing a parallel loading of the

first register with the values set on the parallel load inputs (load switch shown).

To signal to the multichannel scaler, the start of the data acquisition cycle, the 13-bit shift register is decoded by four 4-input AND (74F21) gates. The register cycles through all possible states exactly one time during sequence generation, therefore decoding of any state of the register could be used to signal the cycle start. The most straightforward way to produce a trigger is to AND together all bits of the register. Thus, any time all bits of the register are 1 data acquisition gets triggered. No erroneous triggering is observed when the multichannel scaler is directly hooked up to the decoding AND.

Two signals 180° out of phase are required for driving the modulator. Phase splitting is achieved by simply feeding the output of bit 13 of the sequence generator into a D flip-flop (74F74), which provides as a standard feature a Q and a complementary \overline{Q} output. Two identical push-pull power amplifiers are used for amplifying the logic level output to typically 50 V. Only one amplifier made from two radio frequency power metal-oxide-semiconductor field effect transistors (*mosfet*) (MRF148) are shown in Fig. 3. Switching of the high side transistor with the Q output of the phase splitting D flip-flop (74F74) and the low side with the \overline{Q} output causes the output voltage to swing between the supply voltage of the power amplifier and ground. Identical transistors for low and high side of the driver requires the base drive circuit of the high side to float on the drain of the low side transistor. This condition is achieved with the help of an optocoupler (HPCL7101) that allows coupling of the logic signal from the D flip-flop onto the high side. The input capacitance of the MRF148 is with 50 pF quite small but too large to be driven efficiently by the output of the optocoupler. A current amplifier consisting of four parallel logic OR gates (74AC32) is therefore employed to boost the output current of the optocoupler and drive the gate of the MRF148. An identical optocoupler current booster drive stage is used to drive the gate of the low side transistor. The advantage of this drive circuit lies in the tight tolerances of all the logic elements involved, which makes the use of edge alignment circuitry for guaranteed simultaneous switching of the power transistors unnecessary. Further, the high timing precision of the sequence generator is preserved, which guarantees correct modulation, and as a result a minimum of spectral artifacts.

Driving of the modulation grids' capacitance of ~ 100 pF by the driver leads to excessive ringing and a degraded modulation waveform. Ringing is suppressed by a number consisting of a 660 pF ceramic disc capacitor in series with a 100 Ω resistor, that is placed between the two outputs of the power amplifier at the modulator grid. Under operation, several watts of ac power are converted into heat by the snubber resistor. Efficient heat dissipation in the high vacuum where the snubber is mounted is achieved by clamping of the ceramic support of the carbon film resistor onto an aluminum holder that makes good thermal contact with the vacuum envelope. The rise and fall times of the modulation wave-

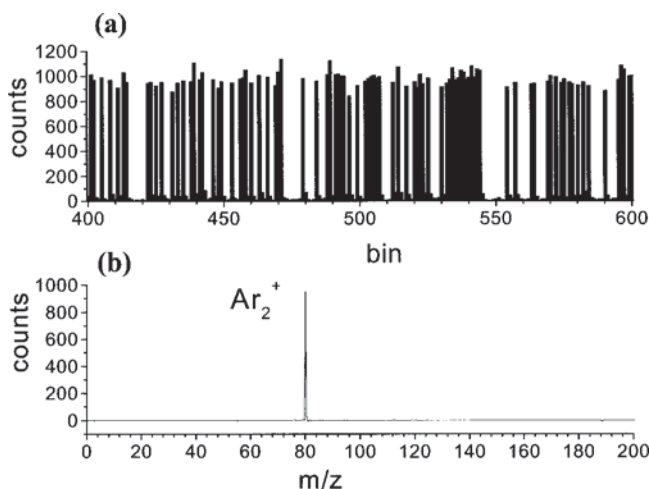


FIG. 4. Portion of the (a) signal waveform and (b) transformed spectrum for the case of an Ar_2^+ ion beam.

form produced by the driver with the load connected were measured to be ~ 10 ns.

IV. RESULTS AND DISCUSSION

A. Single species ion beam

Figure 4(b) shows the mass spectrum of a pure Ar_2^+ ion beam. A corona discharge between the inlet capillary of the electrospray ion source and the skimmer plate in 400 mTorr of argon produces argon ions of which significant numbers react to form Ar_2^+ . The radio frequency amplitude of the ion guides is adjusted to pass only the dimer ion so that an ion beam containing a single species results. This beam is used for diagnostic purposes to reveal the performance of the instrument. Figure 4(a) displays a fraction of the signal waveform of the spectrum, which is shown in Fig. 4(b). The waveform was counted into 100 ns bins, which was the unit time interval used in modulating the beam in the gate mode. For an ion beam of a single species the signal waveform should reproduce the modulation waveform with some time shift depending on the mass-to-charge ratio of the ion. This behavior is clearly observed in Fig. 4(a). Some bins contain approximately 1000 counts whereas others contain almost no counts; the former correspond to a 1 (beam on state) and the latter to a 0 (beam off state) of the modulation sequence. Further, at bin number 537 starts a series of 13 bins of which all correspond to 1's in the modulation sequence. The modulation sequence contains only one subsequence of length 13. This sequence will be clocked out of the shift register as soon as all of its bits are in the 1 state. This state of the register is the one decoded to produce the data acquisition start trigger. Therefore, the flight time of the ions through the instrument must be 537×100 ns or $53.7 \mu\text{s}$. The resolution at this mass can be computed to be $T/(2\Delta t)$ or 268.5. It should be pointed out that this resolution is only observed because a single 100 ns ion packet is collected into a single 100 ns sampling bin. In the worst case a 100 ns ion packet could be sampled equally into two 100 ns sampling bins. The observed width of the peak would then be twice, and the resolution only a half or ~ 134 . The very low number of counts

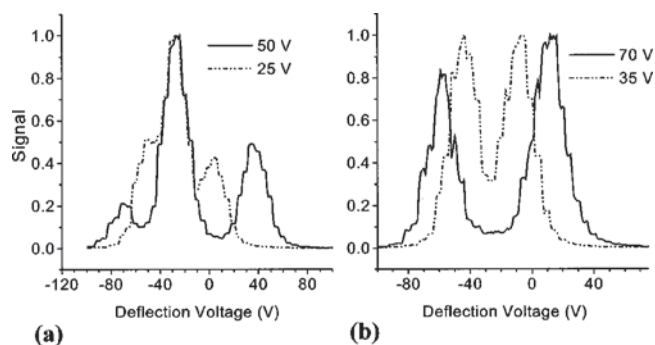


FIG. 5. Time-averaged images of the deflected beams in the detector plane. Data were acquired by scanning of the ion beam over the detector slit by varying the deflection voltage applied to the beam steering plates: (a) gate mode and (b) differential impulse sweep mode. Modulation voltage amplitudes are indicated.

found in the bins corresponding to the beam off state clearly shows that the small beam deflection imparted by the modulating grid is sufficient to switch the beam on and off. Furthermore, no spectral artifacts appear in the spectrum of Fig. 4, which indicates that the imperfect modulation caused by the limited rise and fall time of the voltages at the modulator and the finite deflection region is negligible under the conditions of this experiment.

B. Beam imaging

Additional indications of the proper behavior of the grid modulator can be deduced from beam imaging experiments. The voltages applied to the deflection plates used for beam steering can be scanned. This scanning allows the time-averaged beam image produced in the detector plane to be monitored. Figure 5 shows the beam images acquired with the pseudorandom modulation voltages applied to the grid modulator. Again, the same type of argon ion beam as described above was used in these experiments. The images were acquired by scanning the deflection voltage applied to the vertical deflection plate set from -100 to 100 V at an ion beam energy of 1250 eV. The ion signal was counted into 1 s bins and the deflection voltage was stepped manually every 5 s by 5 V, which explains the stepped structure of the images. When the instrument operates in gate mode we would expect to see in the detector plane a time-averaged image of three equally spaced peaks with an intensity ratio of 1:2:1, because the pseudorandom modulation deflects the ion beam 50% of the time. Furthermore, deflection causes the beam to split into two beams of equal intensity deflected to each side of the undeflected beam. The image acquired in gate mode operation is shown in Fig. 5(a) for two modulation voltages. At a deflection voltage of -30 V the feature from the undeflected beam is seen. A feature of about half this intensity is seen around a deflection voltage of 5 and 35 V for the modulation voltages of 25 and 50 V, respectively, and corresponds to one of the expected deflected bands. For small deflection angles a proportionality exists between the deflection voltages applied to the modulator and the ones applied to the beam steering plates. This behavior implies that the deflection voltage scales in Fig. 5 can be directly mapped into a deflection angle scale. At the 1250 eV beam energy used a

deflection voltage change of 40 V corresponds to a change in deflection angle of $\sim 1^\circ$. The proportionality is clearly seen in Fig. 5(a) where doubling of the modulation voltage also requires doubling of the deflection plate voltage. The second band arising from the deflected beam at more negative deflection voltages than the undeflected feature appears with an intensity considerably lower than expected and at a distance smaller than the one at higher deflection voltage. The reduction in intensity seems to be related to the beam grazing some ion optical element, because it clearly increases with larger deflection angles and is also observed in Fig. 5(b) recorded in differential impulse sweep mode. Nevertheless, this interpretation does not explain why in Fig. 5(a) the deflected features are not located at the same distance with respect to the main feature. The explanation was found with the help of SIMION 6.0 simulations. As it turns out, the asymmetry is caused by a tilt of the grid, normal with respect to the beam axis, which moves both deflected beams more to one or the other side depending on the sense of the tilt. This tilt could be compensated either by tilting the ion beam axis with another set of deflection plates in front of the grid or by properly orienting the grid. The present design of the instrument does not allow either method of correction to be implemented easily. Our results show, nevertheless, that at this stage of development the instrument does work satisfactorily without any correction.

Figure 5(b) shows time-averaged beam images for operation in differential impulse sweep mode. As expected two features of equal intensity appear corresponding to the deflected beams. Again it is observed that the deflection angle is proportional to the applied modulation voltages. Some reduction in intensity is observed at the higher modulation voltage for the feature requiring a more negative deflection voltage as was already observed in Fig. 5(a).

C. Gate and differential impulse sweep mode operation

The differences between gate mode and differential impulse sweep mode, as they were discussed above, are illustrated by the experimental data presented in Fig. 6. Figure 6 shows two traces. The offset trace (a) showing a peak at bin 3424 was recorded in gate mode operation, whereas the trace (b) showing a feature at bin 8517 was recorded in differential impulse sweep mode. Both are positive-ion electrospray ionization spectra of tetraethylammonium bromide from a 1.6×10^{-5} M solution in methanol. The modulation sequence was based on a 10-bit generator, which produces a sequence of length 2047. The circuit was clocked at 10 MHz, which resulted in a 100 ns unit time interval of the modulation sequence. The signal waveform was counted into 20 ns bins so that five acquisition bins were used to cover a unit time interval. Therefore, the total length of the spectrum is 10 235 bins, as seen in Fig. 6. The inverse transform of the signal waveform was carried out in the manner described above using five sets of 2047 bins. The beam energy was 1250 eV for these experiments, and the deflection voltage was 70 V for differential impulse sweeping and 35 V in gate mode. The phase shift occurring in going from gate mode to differ-

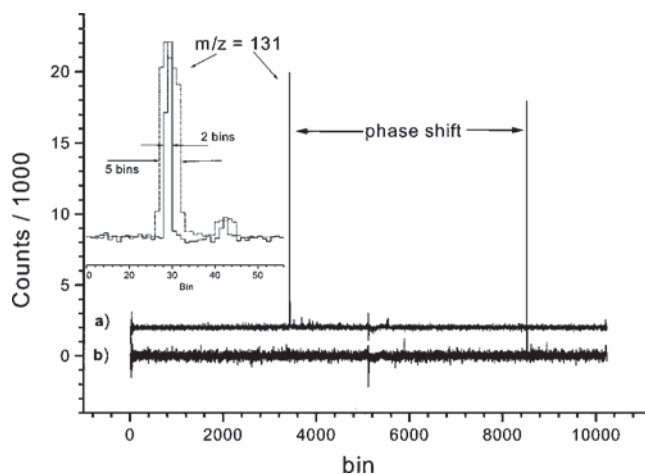


FIG. 6. Electro spray ionization mass spectra of tetraethylammonium bromide in (a) gate mode and (b) differential impulse sweep mode with a unit time interval of 100 ns (10 MHz) and an acquisition bin width of 20 ns. The phase shift introduced between gate and differential impulse sweep mode is seen. The insert shows the overlay of the two peaks and the resolution improvement achieved through the shorter pulses produced by differential impulse sweeping.

ential impulse sweeping is clearly seen in the peak shift between traces (a) and (b). Both spectra were acquired for the same amount of time and scaled to identical peak intensities. The lower duty cycle of the differential impulse sweep spectrum (b) manifests itself in the smaller observed signal-to-noise ratio. Both traces are fairly clean with the exception that a noise feature occurs around bin number 5120, and at the start and the end of the traces. It is important to notice that these noise features do not exhibit the phase shift of the mass peaks and are therefore not the result of an imperfect modulation waveform. Their discrete nature suggests clearly a mechanism that is correlated with the modulation, however. Experiments employing other sequences show similar noise features but at locations that depend on the sequence. Electrical noise in the system produces these nonstatistical noise features. The fast switching of the modulation grid causes radio frequency noise spikes on the electrical ground at any transition of the modulation voltages. Consequently, these noise spikes are correlated to the modulation sequence. The discriminator of the multichannel scaler is adjusted to a level where these noise spikes alone cannot produce erroneous counts. The noise spikes on the ground effectively cause the counting threshold of the multichannel scaler to systematically vary with these spikes. As a result, a larger or smaller fraction of the pulse height distribution produced by the detector will be counted depending on the sign of the spikes. This behavior leads to a systematic modulation of the detected background counts and manifests itself as the observed spectral artifacts. Indeed, as Fig. 7(a) shows, spectral artifacts are reduced at lower modulation voltage levels corresponding to lower ground noise levels. At the same time the signal intensity changes are comparatively small except for modulation voltages below 10 V, indicating that the relative amplitude of the artifacts is reduced. Furthermore, artifact size was also observed to vary with discriminator voltage setting but complete removal of artifacts by raising the

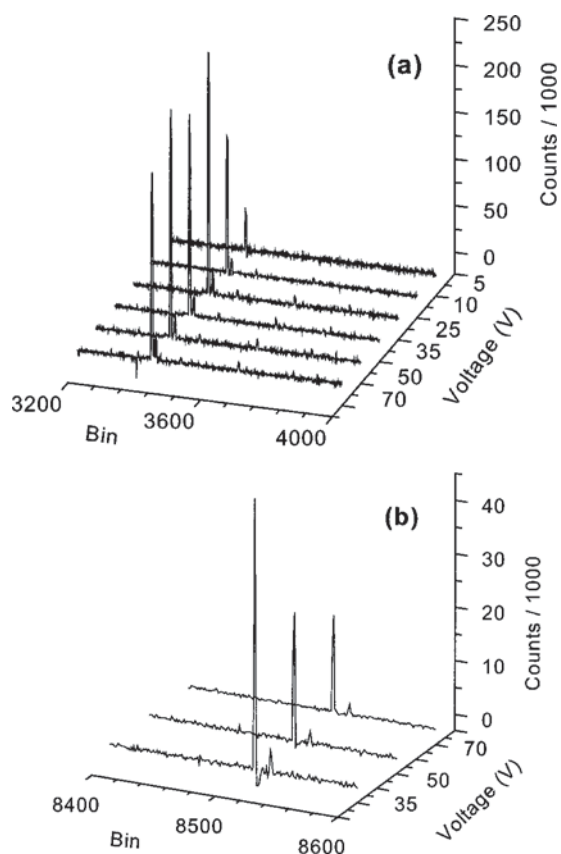


FIG. 7. Spectral changes observed as a function of the modulation voltage amplitude for (a) gate mode and (b) differential impulse sweep mode.

detection threshold was never possible, which is what is to be expected.

The insert in Fig. 6 shows the improvement in resolution that is achieved through the shorter pulses that are produced in differential impulse sweeping. For comparison, the tetraethylammonium ion peaks of trace (a) and (b) are overlaid and expanded. The wider peak acquired in gate mode shows the expected time resolution of 5 bins or 100 ns. This width is reduced to 2 bins or 40 ns for the differential impulse sweep spectrum, which is an improvement by a factor of 2.5 in mass resolution. The small feature at bin 44 in the expansion comes from the ^{13}C (and ^{15}N) isotopes and shows the expected abundance of $\sim 10\%$. The full width at half maximum (FWHM) resolution at 130 m/z (the major peak) is found to be 338 in gate mode and 845 in differential impulse sweep mode.

D. Deflection voltage dependence of spectra

As was already indicated in the previous section, it is desirable to operate the modulator with as small a drive potential as possible to minimize radio frequency noise. Smaller drive voltages also reduce the power necessary to drive the capacitive load presented by the modulator and its snubber. The beam images of Fig. 5 indicate that a deflection voltage of 50 V should fully suffice to achieve complete spatial separation of deflected and undeflected beams in gate mode operation and therefore a maximally modulated signal. The series of spectra shown in Fig. 7(a) at varying deflection

potentials show that actually no real gains in SNR in achieved after the deflection voltage exceeds 25 V. This behavior might look somewhat surprising because the beam image of Fig. 5(a) seems to indicate that full modulation is not achieved at this deflection potential. Two facts should be kept in mind with respect to the beam images. First, the images are convolutions of the true image with the detector slit function. Second, the images are time averages. For both reasons the images are not good indicators with respect to the actual achieved modulation depth. Another point already discussed in the context of Fig. 6 is the increase in spectral artifacts accompanying the increase of drive voltage. Furthermore, it is seen that quite good results are already achieved with a deflection potential of only 10 V. This result is of importance because of the reduced power dissipation and the available faster electronic components that will allow for faster modulation and therefore increased resolution. Theoretically, the full modulation depth is reached when deflected and undeflected beams can be separated to the extent that only ions in the undeflected beam pass the detector slit and produce signal. The factors contributing to this minimum deflection are beam size, beam energy spread, and aberrations in the ion optics. For a monochromatic parallel ion beam and an ideal modulator that deflects all ions independent of their paths by the same angle, a spatial deflection at the detector of the size of the beam width should suffice. The effective path length through the instrument is about 2.9 m. Assuming a relative large ion beam of 5 mm in diameter a deflection angle of $\sim 0.1^\circ$ with respect to the beam normally would suffice. At a beam energy of 1250 eV the transversal energy that needed to be imparted to the ions by the modulator to achieve this condition would be ~ 3.8 meV. This value is about 15% of the mean kinetic energy in a thermal ion beam so that its contribution can be neglected in practical cases. The energy spread of the ion beam exiting the octopole ion guide is larger than $2kT$ because of the variation of the average kinetic energy within the ion guide. The simulated data of Hägg and Szabo³⁷ for the transmission of ions through an octopole lead to an upper estimate of the kinetic energy spread of about 80 meV. From SIMION 6.0 simulations of the modulator it is found that a deflection voltage of 23 V is needed to imparted 160 meV transversal beam energy at 1250 eV, which corresponds to a deflection angle of 0.65° . The good agreement of this number with the 25 V found from Fig. 7(a) might be somewhat fortuitous, but the agreement does indicate that the transverse energy spread dominates the necessary deflection voltage and that the additional contribution by aberrations of the ion optics can be neglected.

Figure 7(b) shows the changing spectral appearance when the modulation voltage is increased when the instrument is operated in differential impulse sweep mode. An increase in the deflection voltage reduces the signal intensity, but at the same time a significant reduction in baseline noise is observed caused by the reduction of the number of background counts. It was found that 50 V or more are necessary to optimize the spectral quality. As expected, this value is twice the 25 V found for gate mode operation. Comparison of Figs.

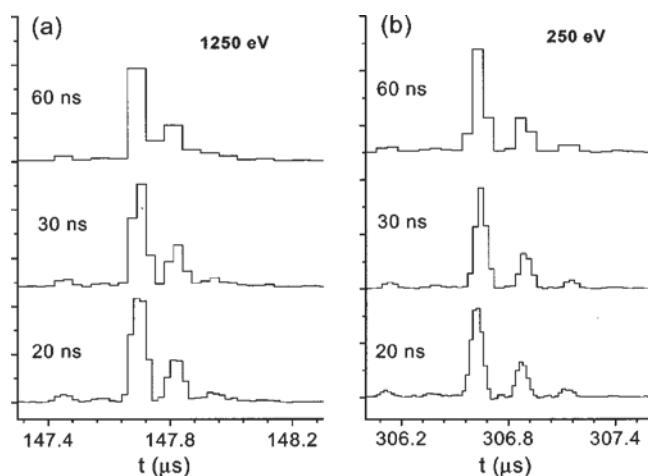


FIG. 8. Effect of the sampling bin width on the appearance of the protonated isotope cluster of reserpine (MW 608.68 g/mol). The unit time interval of the modulation sequence was 60 ns. Traces for sampling into 60, 30, and 20 ns bins are shown from top to bottom at beam energies of (a) 1250 eV and (b) 250 eV.

7(a) and 8(b) shows the improved resolution achieved in the differential sweep mode [Fig. 7(b)].

E. Resolution, sampling, and mass cutoff

If the duty cycle of the instrument does not depend on the repetition rate, it is desirable to operate at the lowest possible beam energies to increase the flight time and with it the mass resolution. Also, in theory, a reduction in beam kinetic energy allows the deflection voltages to be reduced, which again makes it easier to modulate faster and achieve even higher resolution. Detection limits ($S/N=3$) for peptides were found to hover in the 1–10 fmol range and in exceptional cases even smaller amounts could be detected.³⁸ Figures 8(a) and 8(b) show two series of spectra of reserpine (MW 608.7 g/mol) recorded at beam energies of 1250 and 250 eV, respectively. Spectra were acquired in gate mode with a unit time modulation width of 60 ns. Sampling was into 60, 30, and 20 ns bins, as indicated in Fig. 8. The spectra show that an increase in the sampling rate does not increase the time resolution and therefore mass resolution. The peak definition is improved at higher sampling rates, which allows a more accurate location of the peak maximum and a better mass accuracy to be achieved. Figure 8 also shows that the isotope cluster is resolved. The FWHM resolution at 250 eV is 1980, which is almost two times the value (1044) measured at a 1250 eV beam energy. The improvement in resolution is slightly less than what would be expected from the lengthened flight time.

The mass spectrum of gramicidine S (MW 1141.4 g/mol) could be acquired at a beam energy of 1250 eV with a resolution of 2200 for the $(M+H)^+$ ion in gate mode. Attempts to improve the mass resolution further by employing differential impulse sweeping or decreasing the beam energy failed, however. Simulations carried out with SIMON 6.0 of the grid modulator showed that this failure is caused by the introduction of excessive kinetic energy spread into the ion beam through the modulation process. For the modulation to really resemble the 0 and 1 pattern of the pseudoran-

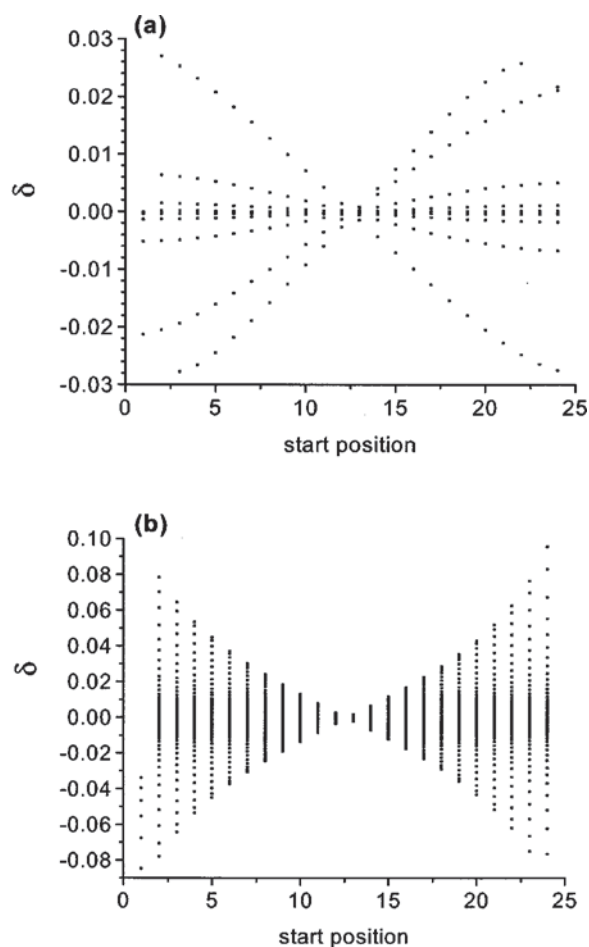


FIG. 9. Fractional beam energy spread δ as a function of the fractional starting position between modulator wires. Wires are located at positions 0 and 1. Center-to-center wire distance is $158.75 \mu\text{m}$, and wire diameter is $20 \mu\text{m}$. Simulations were carried out at 250 eV beam energy and a square wave modulation for two periods (200 ns) was applied to the modulator: data for an ion beam of (a) 10 m/z and (b) 1000 m/z. Points lying on lines correspond to ions that were started simultaneously but at different locations. Each plot contains approximately 2500 data points. Ions were selected that had deflection angles of less than 1.7° after passing the modulator.

dom sequence it is essential that beam switching occurs on a time scale much smaller than the actual minimum pulse duration. One limit on the switching times is set by the rise and fall times of the voltages applied to the modulator, which are ~ 10 ns with the driver described in the experimental section. Another limit is set by the mass of the ions making up the ion beam to be switched. This second limitation arises because the region in which the deflection occurs is finite and ions of higher mass have a larger transit time through this region. As a consequence, the number of ions affected by the switching process will increase with mass. In addition, the energy spread introduced into the beam will be larger for heavier ions. The simulated data presented in Fig. 9 illustrates this behavior. The modulator was modeled as an interleaved comb of infinitely long wires, which allows the device to be simulated within SIMION 6.0 by a two-dimensional potential array. The fields were terminated by electrodes parallel to the grid at a distance of two wire spacings from the modulator. The wires were spaced $158.75 \mu\text{m}$ apart, as in the experimental device. To understand more fully the instru-

ment effects, an ideal ion beam was simulated by spacing ions uniformly every $6.35 \mu\text{m}$ along one terminating electrode to cover the distance between two wires of the grid (26 ions). Ions were started with exactly 250 eV every 1 ns along the normal of the grid plane. A square wave modulation with an amplitude of 25 V and a period of 100 ns was applied to the wires, which produces a sequence of pulses of 50 ns duration. The rise and fall of the potentials was modeled by as a linear rise or fall of the voltages within a 10 ns time interval at each transition. A total of 5200 trajectories covering a time interval of 200 ns were computed for each waveform. The kinetic energy component of each ion along the grid normal was used to calculate the time-of-flight through a focused single-stage reflectron mass spectrometer³⁹ with the same effective path length of 2.9 m as our instrument. Arrival times of trajectories with a deflection angle smaller than half the full angle of deflection (3.4°) with respect to the normal were selected to simulate the detector slit.

Figures 9(a) and 9(b) show plots of the fractional spread in beam energy δ as a function of initial position for ions of 10 and 1000 m/z. The fractional spread δ is defined as kinetic energy along the grid normal after passing the modulator minus the nominal beam energy (250 eV) divided by the nominal beam energy. The line drawn in Figs. 9(a) and 9(b) connect ions starting at the same time. Each of the two panels contains about 2500 data points. Most of these points fall in a narrow horizontal region around a δ of 0 where they overlap. The points outside this region are from ions that acquired substantial δ owing to the fact that they were between the modulator wires during a switching of the potentials. Comparing the two panels we notice that the number of ions that acquired a substantial δ ($\delta > 0.005$) and the magnitude of δ is much larger for a m/z of 1000 as compared to a m/z of 10. Furthermore, for ions starting at the same time the value of δ changes almost linearly with position from a maximum for ions close to a wire to zero at the center between wires. The straightforward explanation for this behavior is that the acquired δ or change in kinetic energy of an ion is equal to the change in potential of its trajectory during its flight through the deflection region. Because the voltages on the wires are changed at any time by the same amount but with opposing signs the potential in the center between wires does not change, even during the switching of voltages to the wires. Therefore, no change in kinetic energy is observed for ions traveling through the center between the wires. The ion trajectories through the modulator are essentially straight because of the small deflection angles that are achieved. The maximum expected potential change occurs very close to the wires and will be of the size of the modulation voltage. The modulation voltage of 25 V used in simulating the data corresponds to a maximum δ of 0.1 at 250 eV beam energy. This large a value of δ can only be acquired by ions traveling slowly enough and close by a wire. This is the reason why some of the 1000 m/z ions in Fig. 9(b) are observed to acquire a value of δ of 0.08 close to the maximum, whereas the maximum value of δ acquired in Fig. 9(a) is only 0.028. The almost linear change of δ across a wire spacing allows the wire modulator to be treated like an ideal set of deflection plates producing a homogeneous field in between the plates

over a distance of the plate length l . The corresponding plate length can be calculated from the transit time, which from the data presented is about 2 ns for a 10 m/z ion at 250 eV, resulting in an effective plate length l of about $139 \mu\text{m}$, which is 0.875 wire spacings. The possibility to treat the wire comb modulator for small deflection angles as an ideal set of deflection plate is of great value. It allows the simulation of the Hadamard transform time-of-flight mass spectrometer to be carried out without invoking trajectory integration routines.

The effects described here are not to be confused with the tilting and bending of the isochronous plane described for conventional time-of-flight instruments when ions pass between deflection plates^{11,40,41} to which static potentials are applied. Here the change of the potentials applied to the modulator introduces beam kinetic energy spread. These dynamic effects are much larger than the static ones described.

Figures 10(a) and 10(b) show the fractional kinetic energy spread as a function of the flight time through the simulated single-stage reflectron instrument as well as the binned arrival time distribution for a m/z of 10 and 1000, respectively. Again, it is seen that at 10 m/z only a small fraction of ions at the pulse edges are affected. The introduced spread is also within the compensation capabilities ($\delta < 0.03$) of a single-stage reflector, so that the modulation waveform is nicely reproduced as the binned time-of-flight distribution shows. For a m/z of 1000 the spread introduced to a large fraction of the ions exceed clearly the capabilities of a single-stage mirror. The binned time-of-flight distribution shows the distortion of the square modulation into pointed peaks with long tails. These tails reduce the signal level and produce at the same time an increased background; both effects reducing the achievable signal-to-noise ratio.

It should be noted that the energy spread introduced by beam modulations is much larger than the 80 meV estimated for the ion beam emerging from the ion source, so that this spread can be neglected in the current discussion. The tailing and peaking observed in Fig. 9(b) would be smoothed out more if the arrival times were counted into 50 or 25 ns bins, which would be a more typical bin width in an actual experiment. The degrading effects observed in the waveform of Fig. 10(b) will not be observed with the same severity throughout a pseudorandomly modulated signal waveform because energy dispersion is only introduced when the potentials to the modulator are switched. Consecutive pulses require potential switching only at the start of the first and last pulses. The energy spread of the pulses sandwiched in between the first and last ones and therefore their distortion will be effectively nil compared to that of the bracketing ones. Overall nonstatistical modulation of pulse and background intensities will be observed in the signal waveform, which translates into increased statistical and nonstatistical noise in the inverse transform of the signal. The nonstatistical noise becomes more visible in spectra recorded at higher sampling rates, because the different sets of bins for which an inverse transform must be taken so that the resulting spectra are assembled into the full mass spectrum are affected to varying degrees.

So far, the discussion has focused on gate mode opera-

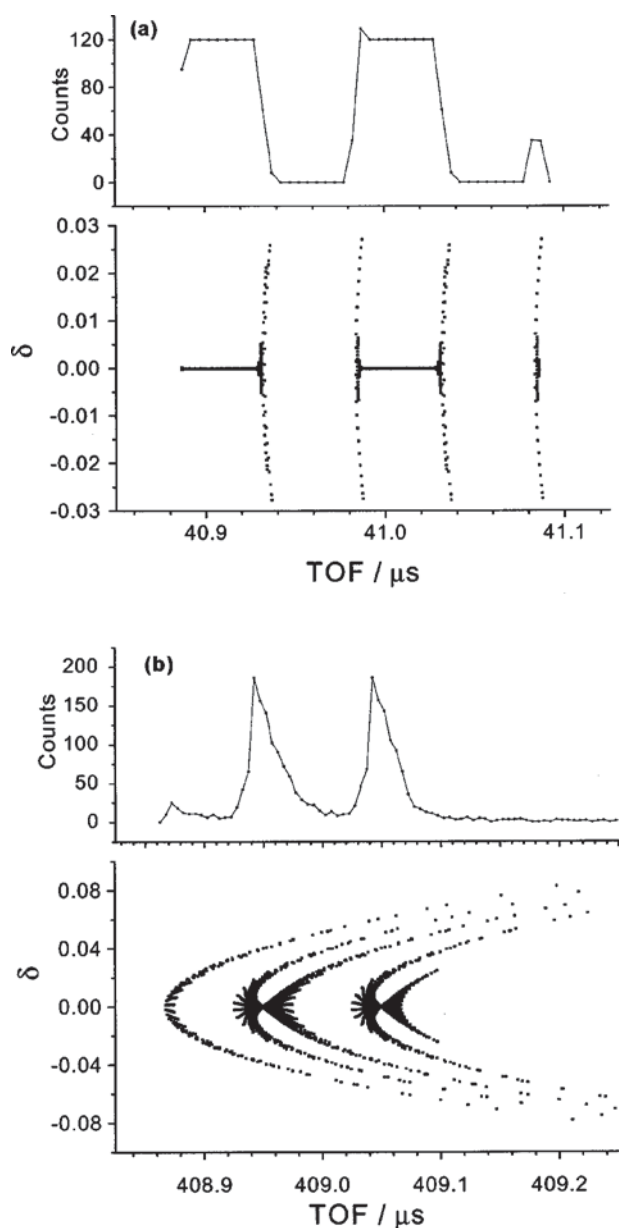


FIG. 10. Fractional kinetic energy spread δ as a function of the arrival time after passing through a single-stage reflectron mass spectrometer of effective path length 2.9 m. Beam energy was 250 eV: data for (a) 10 m/z ions and (b) 1000 m/z ions. The same data set is displayed as in Fig. 9. Top trace is obtained by counting data shown on the bottom into 5 ns bins.

tion and not much needs to be added to understand what happens in differential impulse sweep mode. Similar simulations carried out for a modulator operating in the differential impulse sweep mode show that a much larger number of ions will receive an energy spread to begin with, because the pulses are formed during the time the potentials of the modulator wires change. Worse still, to achieve the same deflection angle, modulation voltages must be doubled, which causes doubling of the maximum value of δ . This feature prevents the expected increase in resolution through the production of short pulses by beam sweeping to be realized with a single-stage mirror at low beam energies. This conclusion is in agreement with our inability to produce spectra by differential impulse sweeping at 250 eV. At the higher beam energy of 1250 eV, spectra could be generated for m/z values

below 250, but even the resolution improvements were observed to deteriorate rapidly above 100 m/z.

Improvement in the instrument performance requires that the number of ions affected by the modulation is further reduced in gate mode and the magnitude of the introduced beam kinetic energy spread is reduced in size or compensated for in both gate and differential impulse sweep modes. For a given mass, an increase in the beam kinetic energy reduces the ion transit time through the modulator which causes less ions to be affected in the beam switching process in gate mode and potentially δ to be reduced as well. But, the improvement that is achievable is limited because the velocity of the ions increases only as the square root of the energy. Increasing the beam energy further demands a proportional increase in the deflection potentials if the deflection angle is to be kept constant, which causes a proportional increase in δ instead of a reduction. Last, increased beam energy will reduce the flight time and therefore the mass resolution. Therefore, it turns out that the requirement for a minimum deflection angle that physically separates deflected and undeflected beams in space couples beam energy and deflection potentials in a fashion that makes adjustment of these parameters ineffective for making a marked improvement in the performance of this instrument. This reasoning forces us to consider how to compensate for the detrimental effects of the introduced δ through a higher-order correction in the arrival times, which suggests the use of a double-stage, curved-field or even a quadratic-field reflector. Shortening the distance between the wires of the modulator can significantly reduce the number of ions actually affected in gate mode operation because a reduction in distance between wires will proportionately reduce the effective deflection region of the device. Thus, a device possessing a wire spacing of 40 μm , which is about four times smaller than our present device, will have a 16 times higher mass cutoff. In such a device, the waveform in Fig. 9(b) for a 1000 m/z ion beam is expected to resemble one acquired for a 62.5 m/z ion beam with the present device. Although no data are shown, the waveform would look very similar to the one in Fig. 10(a) only showing a little tailing to longer times. Hence, HT-TOFMS instruments should be significantly improved by the fabrication of interleaved comb modulators whose oppositely charged elements are more closely spaced than what we have assembled by hand.

Experimental and simulated data indicate that a high-mass cutoff exists for the described Hadamard transform time-of-flight mass spectrometer. This cutoff starts to appear very gradually and manifests itself by an increase in statistical and nonstatistical noise in the spectra with increasing mass. A consequence of the multiplex nature of the experiment is that this noise source limits the quality of the low-mass region, because noise produced in a single channel spreads out uniformly over the spectrum.

The modulation action of the comb modulator device can be quite accurately described as that of a set of ideal deflection plates with a plate length of about 0.875 wire spacings. Modulation becomes more ideal as the plate length is reduced, which suggests to us that the production of micromachined grids using current micromachining capabilities

should extend the mass range by a factor of up to 50.

The energy spread introduced into the beam along the flight axis by the modulator restricts the obtainable resolution and mass range in the differential impulse sweep mode that can be obtained in the current instrument. The maximum fractional kinetic energy spread is expected to be even under optimum conditions 0.15. This value exceeds the compensation capabilities of the single-stage reflector used in the present instrument and does not allow this type of experiment to be carried out efficiently. High-order correction of the arrival times is possible however, with curved and quadratic field reflectors. This modification should allow for FWHM mass resolutions $m/\Delta m$ of 20 000 to be achievable at 1000 m/z in a Hadamard transform TOFMS instrument of the current size according to our estimates. We believe that such an instrument would extend significantly the use of time-of-flight mass spectrometry as applied to ion sources having extended or continuous ion streams.

ACKNOWLEDGMENT

This work was supported by Beckman Coulter, Inc.

- ¹L. Bewig, U. Buck, S. R. Gandhi, and M. Winter, *Rev. Sci. Instrum.* **67**, 417 (1996).
- ²G. Comsa, R. David, and B. J. Schumacher, *Rev. Sci. Instrum.* **52**, 789 (1981).
- ³D. L. Price and K. Sköld, *Nucl. Instrum. Methods* **82**, 208 (1970).
- ⁴J. Viehhaus, L. Avaldi, F. Heiser, R. Hentges, O. Gessner, A. Rudel, M. Wiedenhoft, K. Wieliczek, and U. Becker, *J. Phys. B* **29**, L729 (1996).
- ⁵R. J. Cotter, *Time-of-Flight Mass Spectrometry*, ACS Symposium Series 549 (American Chemical Society Washington, DC, 1994).
- ⁶R. J. Cotter, *Time-of-Flight Mass Spectrometry* (American Chemical Society Washington, DC, 1997).
- ⁷A. Brock, N. Rodriguez, and R. N. Zare, *Anal. Chem.* **70**, 3735 (1998).
- ⁸L. Fang, R. Zhang, E. R. Williams, and R. N. Zare, *Anal. Chem.* **66**, 3696 (1994).
- ⁹A. N. Verentchikov, W. Ens, and K. G. Standing, *Anal. Chem.* **66**, 126 (1994).
- ¹⁰W. C. Wiley and I. H. McLaren, *Rev. Sci. Instrum.* **26**, 1150 (1955).
- ¹¹A. F. Dodonov, I. V. Chernushevich, and V. V. Laiko, in *Time-of-Flight Mass Spectrometry*, edited by R. J. Cotter (American Chemical Society, Washington, DC, 1994), Vol. 549, p. 108.
- ¹²J. Hoyes (personal communication, 1999).
- ¹³A. F. Dodonov, Proceedings of the 47th American Society for Mass Spectrometry Conference on Mass Spectrometry and Allied Topics, ASMS'99, Poster ThOC2.
- ¹⁴J. M. B. Bakker, *J. Phys. E* **6**, 785 (1973).
- ¹⁵J. M. B. Bakker, *J. Phys. E* **7**, 364 (1973).
- ¹⁶G. E. Yefchak, G. A. Schultz, J. Allison, C. G. Enke, and J. F. Holland, *J. Am. Soc. Mass Spectrom.* **1**, 440 (1990).
- ¹⁷G. Wilhelmi and F. Gompf, *Nucl. Instrum. Methods* **81**, 36 (1970).
- ¹⁸M. D. Harwit and N. J. Sloane, *Hadamard Transform Optics* (Academic, London, 1979).
- ¹⁹E. D. Nelson and M. L. Fredman, *J. Opt. Soc. Am. A* **60**, 1664 (1970).
- ²⁰R. N. Bracewell, *The Fourier Transform and its Applications*, 2nd ed., McGraw-Hill series in Electrical Engineering, Circuits and Systems (McGraw-Hill, New York, 1986).
- ²¹A. G. Marshall, *Fourier, Hadamard, and Hilbert Transforms in Chemistry* (Plenum, New York, 1982), pp. 562.
- ²²A. G. Marshall and F. R. Verdun, *Fourier Transforms in NMR, Optical, and Mass Spectrometry* (Elsevier, Amsterdam, 1990).
- ²³C. V. Nowikow and R. Grice, *J. Phys. E: Sci. Instrum.* **12**, 515 (1979).
- ²⁴P. Zeppenfeld, M. Krzyzowski, C. Romainczyk, and R. David, *Rev. Sci. Instrum.* **64**, 1520 (1993).
- ²⁵J. L. Buevoz and G. Roult, *Rev. Phys. Appl.* **12**, 591 (1977).
- ²⁶J. L. Buevoz and G. Roult, *Rev. Phys. Appl.* **12**, 597 (1977).
- ²⁷A. Ahmad and A. M. Elabdalla, *Computers Elect. Engin.* **23**, 33 (1997).
- ²⁸P. Horowitz and W. Hill, *The Art of Electronics*, 2nd ed. (Cambridge University Press, Cambridge, 1989).
- ²⁹D. D. Koleske and S. J. Sibener, *Rev. Sci. Instrum.* **63**, 3852 (1992).
- ³⁰A. N. Krutchinsky, I. V. Chernushevich, V. L. Spicer, W. Ens, and K. G. Standing, *J. Am. Soc. Mass Spectrom.* **9**, 569 (1998).
- ³¹D. A. Dahl, SIMION 3D, VERSION 6.0, Idaho National Engineering Laboratory, 1995.
- ³²A. M. Cravath, *Phys. Rev.* **33**, 605 (1929).
- ³³N. E. Bradbury and R. A. Nielsen, *Phys. Rev.* **49**, 388 (1936).
- ³⁴R. Weinkauff, K. Walter, C. Weickhardt, U. Boesl, and E. W. Schlag, *Z. Naturforsch. A* **44A**, 1219 (1989).
- ³⁵C. W. Stoermer, S. Gilb, J. Friedrich, D. Schooss, and M. M. Kappes, *Rev. Sci. Instrum.* **69**, 1661 (1998).
- ³⁶P. R. Vlasak, D. J. Beussman, M. R. Davenport, and C. G. Enke, *Rev. Sci. Instrum.* **67**, 68 (1996).
- ³⁷C. Hägg and I. Szabo, *Int. J. Mass Spectrom. Ion Processes* **73**, 295 (1986).
- ³⁸N. Rodriguez, Ph. D thesis, Stanford University, 1999.
- ³⁹T.-I. Wang, C.-W. Chu, H.-M. Hung, G.-S. Kuo, and C.-C. Han, *Rev. Sci. Instrum.* **65**, 1585 (1994).
- ⁴⁰M. Gilhaus, *J. Am. Soc. Mass Spectrom.* **5**, 588 (1994).
- ⁴¹T. Dresch, Proceedings of the 46th American Society for Mass Spectrometry Conference on Mass Spectrometry and Allied Topics, ASMS'98, Poster THP033.